# Supporting Information

## Mesoscale Superlubric Brownian Machine based on 2D graphitic interfaces

Keren Stein, Gautham Vijayan, Ron Bessler and Elad Koren*

*Faculty of Materials Science and Engineering, Technion – Israel Institute of Technology, 3200003 Haifa, Israel.*

**Email: eladk@technion.ac.il*

**Table of content:**

## A. Sample fabrication

Freshly cleaved bulk HOPG was spin coated with polymethyl methacrylate (PMMA) photoresist. Electron beam lithography (Raith EBPG 5200) was employed to define the pillar shape onto the photoresist coated substrate. A short oxygen plasma was used to clean the resist residuals prior to metal deposition. The metal deposition was carried out by electron beam evaporation (Evatec BAK-501A) – 5 nm of Cr were deposited to form good adhesion, followed by 25 nm Ni, and 25 nm Au. The photoresist was lifted off from the substrate using acetone, and the final pillar structures were formed using reactive ion etching (RIE- Plasma-Therm 790). Oxygen plasma was used to etch the HOPG (200 W, 20 sccm and 20 mT). Detailed schematics of the aforementioned process is described below.

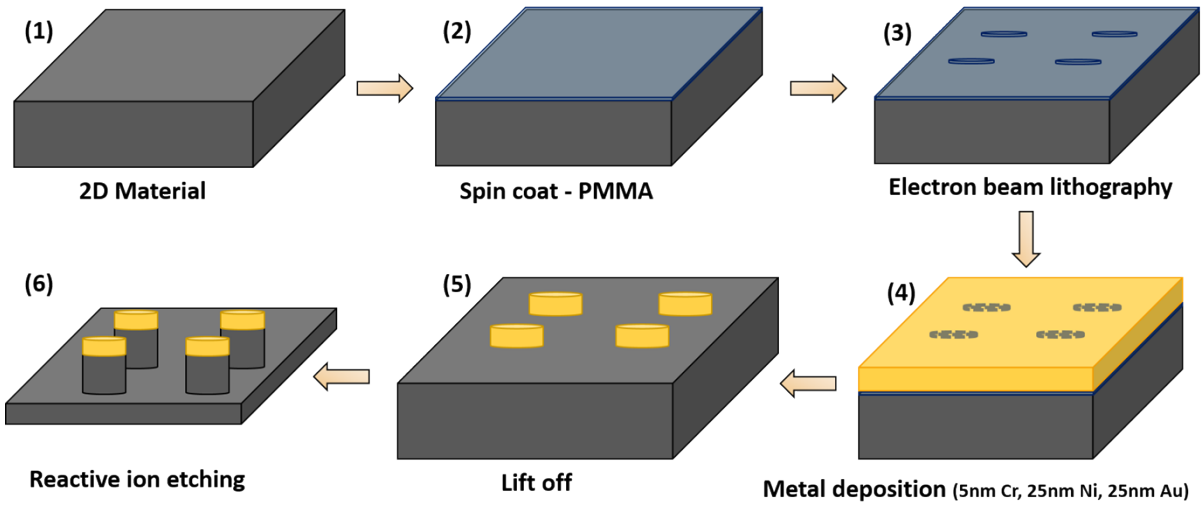


Supplementary Figure 1. Schematics of the steps involved in fabrication proces. (1) Pristine HOPG. (2) Spin coating is performed on the substrate to cover with PMMA as photoresist. (3) Electron beam lithography is employed to write circular as well as bearing pillar structures for nanomanipulation. (4) Metal depostion is performed on the entire substrate. (5) Lift off process results in metal pillars precisely at the patterened positions. (6) RIE process produces pillar structures of 2D materials with metal contacts serving as the etch mask.

## B. Tip calibration and adhesion force analysis

Calibration of the lateral force constant of the AFM cantilever was done by using the adhesion energy of graphite ($\sigma$ = 0.227 J/m$^2$) (*1*). In essence, during the sliding process, new interfacial area is created which is opposed by the line tension forces arising from the interfacial energy (Supplementary Fig. 2). The line tension force acting along the slide direction can be defined as (*1*),

$$F = \sigma \frac{dA}{dx} \tag{S1}$$

where $\sigma$ denotes the adhesion energy per unit area, $A$ is the overlapping area between the mesa sections and $x$ denotes the distance moved along the sliding direction from the initial position. For a circular mesa with a radius of $r$, the instantaneous overlapping area ($A$), can be described as,

$$A(x) = 2r^2\left[\cos^{-1}\left(\frac{x/2}{r}\right) - \frac{x/2}{r}\sqrt{1-\left(\frac{x/2}{r}\right)^2}\right] \tag{S2}$$

Equation S1 can be rewritten by substituting for $A$ from equation S2 as (*1*),

$$F(x) = -2\sigma r\sqrt{1-\frac{(x/2)^2}{r^2}} \tag{S3}$$

For relatively small lateral displacement i.e. $x < r$, the cantilever experiences relatively constant force during the shearing process. Hence, the lateral force at the onset of shearing can be directly related with the known radius $r$ and $\sigma$ based on the following expression (*1*),

$$F_A = 2\sigma r \tag{S4}$$

Consequently, the lateral force constant $c$ can be used to convert the measured lateral deflection from volts to Newton by substituting the known adhesion energy $F = 2\sigma r = c \times V$. The obtained lateral force constant is employed to convert the lateral deflection from volts to nano Newton (nN) in further shearing experiments.

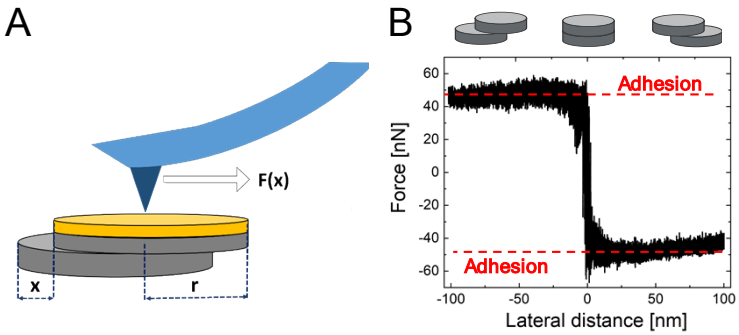


Supplementary Figure 2. (A) Schematic of the adhesion measurement. $r$ denotes the pillar radius. The sliding distance from the initial position is defined as $x$ and the corresponding sliding force experienced by the cantilever is $F(x)$. (B) Typical force versus distance curve, where the force is relatively constant for $x < r$ and therefore the average force (marked by red dashed line) can be used to calibrate the spring constant in case the adhesion energy in known or to extract the adhesion force once the force constant of the cantilever is known (based on equation S4).

### C. Shearing procedure

The sample was fixed to a Bruker Dimension V AFM stage by magnets. Precise electromechanical manipulation was performed using nanolithography scripts in C++ language. First, the desired nanostructure was located using AFM tapping mode. Subsequently, the script implemented the following steps: cold-welding the tip to the metal mask to establish a strong mechanical contact, then shearing and sliding the pillar. To establish an appropriate cold-welding effect between the metal-coated Si AFM tip (PPP-EFM-50, normal force constant ~ 4 N/m) and the sample surface, a normal load of 50 nN and an electrical voltage pulse of 4 V for 1 s were applied. The lateral force was recorded for sliding velocities of 50, 250, 1250, 5000, 25000, 50000, 100000, 250000, 5000, 50 nm/s. The lateral deflection signal was taken directly from the AFM controller and was recorded by a Keysight Oscilloscope (500 MHz, Infiniium S Series) with a constant sampling rate of 200 kHz (time resolution of 5 μsec).

For each velocity the sliding cycle included movement of 100 nm to the right, 200 nm to the left and finally 100 nm back to the original position. The friction force was calculated for the displacement of the top mesa structure to the left and right sides with respect to the fully overlap position and considered as the force difference between trace and re-trace movements. The adhesion was calculated as the difference between the average positive force (measured while the mesa was sheared to the left) and the average negative force (measured while the mesa was sheared to right) divided by two.

Supplementary figure 3 presents the FFT spectra for both 50 nm·sec$^{-1}$ and for a static case, in which the tip is cold-welded to the top part of the mesa before the slid begins. It can be observed that in both cases there is a distinct peak at 50 kHz, which we attribute to the resonance of the cantilever. In contrast, in the low frequency regime, where we expect to see peaks associated with the hopping distance i.e. ~ 500 Hz, it is evident that there are no peaks for the static case. This further supports our hypothesis that the observed peaks are indeed associated with hopping and not to mechanical noise.

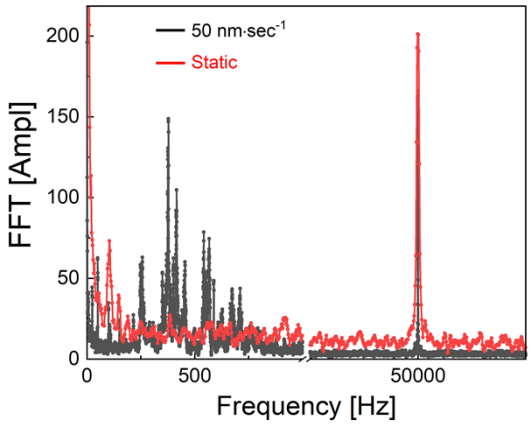


Supplementary Figure 3: FFT analysis for the cases where the tip is connected to the top part of the mesa structure in static (red) and during sliding with a velocity of 50 nm·sec$^{-1}$ (black).

### D. Simulations of bilayer graphene sliding

We used the analytical model developed by Kolmogorov et al. (*2*) to calculate the potential landscape and the forces acting on the atoms for circular graphene bilayer stacks with radii *r* of 5 nm. The model accurately predicts the experimentally measured mean value of the interface energy (*1*). In the simulation, the bottom reference layer is centered at a hollow site position and the coordinate frame is oriented such that the x-axis points along an arm-chair orientation and correspondingly the y-axis points along a zig-zag orientation of the graphite lattice. The second layer is initially positioned in an AB stacking configuration with respect to the bottom layer at a fixed vertical offset of 0.335 nm corresponding to the interlayer spacing in bulk graphite. Mesa sliding is simulated by laterally displacing the circular top layer along the *x* coordinate axes. We calculate the binding energy for each atom in the overlapping area as a function of the sliding distance and derive the lateral forces acting on the atoms by taking the derivative of the energy with respect to sliding distance. For a commensurate system with $0^o$ rotation between the sheets the sliding force exhibits giant fluctuations which scale with the overlap area as a result of the commensurate motion of the atoms. The fluctuation amplitude is on the order of ~ 35 pN per atom yielding a maximum force at the beginning of the slide of 0.12 μN for a radius of 6 nm and 84 μN for a mesa radius of 100 nm (*1*, *3*). These values are orders of magnitude larger than the respective mean line tension forces obtained from the simulation and measured experimentally. Similarly, our previous analysis of the friction versus contact area indicated that the misfit angle is between 5-10 degrees (*1*).

Energy dissipation arises from a Tomlinson mechanism due to the compliance of the sliding actuator and due to the in-plane lattice compliance. The latter is neglected here because of the huge value, ~1 TPa of the in plane elastic modulus (*4*). Therefore, the simulated sliding assumes perfectly rigid control of the layer displacement. In addition, the sliding interface is very well supported by the macroscopic top and bottom mesas structures, effectively allowing to neglect out-of-plate lattice distortions.

Based on our previous analysis of the statistical pattern of the measured friction force and the power law of exp $^{-1/5}$ scaling of the force fluctuations (*1*), we inferred that the rotation angle is not a fixed quantity but rather it is subjected to random fluctuations. This mechanism introduces an unpredictable stochastic element rendering trace and retrace pathways intrinsically statistically independent. This interpretation is corroborated by our model simulation in which we allow the top layer to move orthogonally to the sliding direction and to change its rotation angle in order to minimize the interface energy during sliding. The actual trajectory is therefore based on the Boltzmann distribution weights of the potentially available adjacent position states.

In particular, the simulation is implemented in the following way: assuming sliding along the *x*-axis and starting from an initial position $X_0 = (x_0; y_0; \Phi_0)$ the interface energy $E_0$ is calculated. In the next step, the spring base velocity in the *x*- direction was kept constant, whereas the top layer was allowed to move along the *x*-axis by an amount within the range of ± 4 Å with 1 Å increments. Similarly, the Y

and Φ positions were allowed to adjust within the range of ± 0.2 Å with 1 Å increments. Interface energies $E_{xy\phi}$ are calculated for all virtual displacement options, where for each path option the energy difference $\Delta E_{xy\phi} = E_{xy\phi} - E_0$ is calculated and a path probability $P_{xy\phi} = \exp(-\Delta E_{xy\phi}/(k_B T))$ is assigned to allow for thermal fluctuations. The actual path is chosen randomly according to the path probability. The model thus entails an intrinsic thermally activated randomness. Previous comparison between the calculated power spectra and the FFT of the measured lateral force signal indicated that the force fluctuations manifest the intricate interfacial interaction between the adjacent graphene lattices and for the presence of an angular mismatch within the range of 5-15 degree (*1*). This analysis is in excellent agreement with our current FFT analysis for different sliding velocities. Similarly, the analysis of edge versus area conductivities of similar twisted graphitic structures revealed the same misfit characteristics (*5*).

**A. Simulated force versus distance profiles for initial conditions of 10 deg angular mismatch angle**

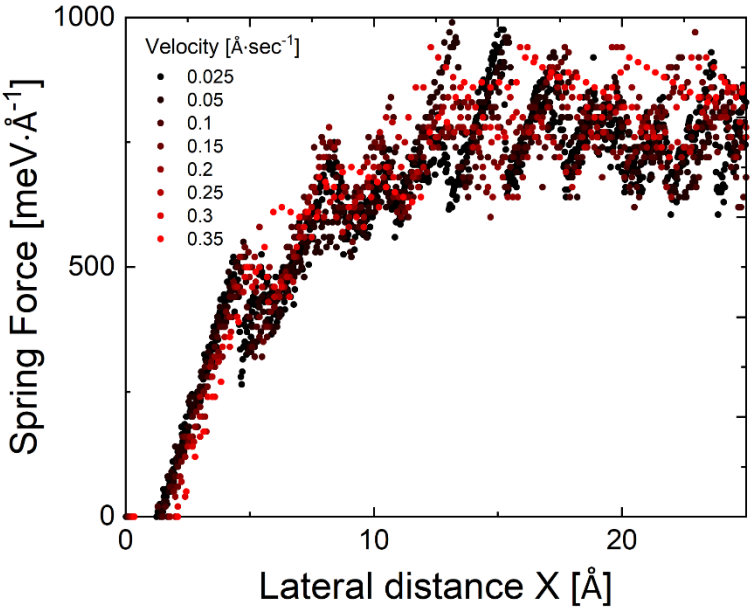


Supplementary Figure 4: Simulated Force versus distance profiles for different velocities conditions for 100 Å diameter bilayer graphene interface during shearing from the center position (full overlap). The initial misfit angle and the Y-position offset were set to 10 deg and zero, respectively.

## B. Simulated results for initial conditions of 20 deg angular mismatch angle

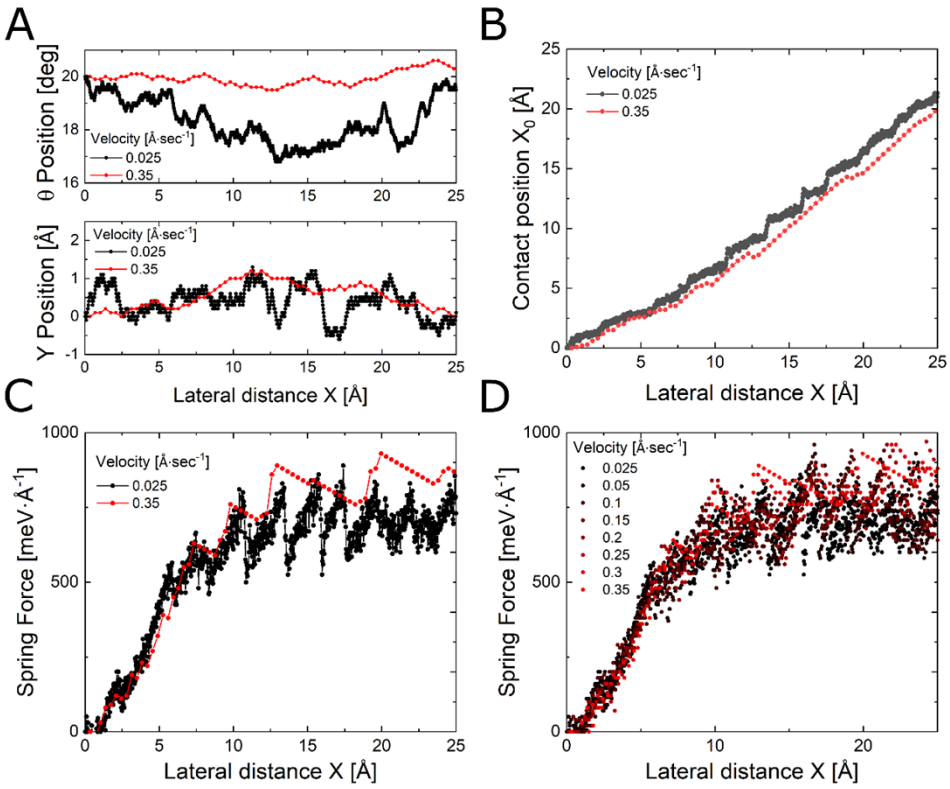


Supplementary Figure 5: Simulated results for different velocities conditions for 100 Å diameter bilayer graphene interface during shearing from the center position (full overlap). The initial misfit angle and the Y-position offset were set to 20 deg and zero, respectively. **(A)** Y-position and rotation misfit angle θ during the slide. **(B)** $x_0$-position of the top flake during the slide. At low velocity of 0.025 Å·sec$^{-1}$, the spring tends to jump forward earlier during the slide and therefore it is overall more relaxed compared to high velocity case of 0.35 Å·sec$^{-1}$. **(C)** Force versus distance profile, where the force profile of the higher velocity case follows the maximal values of the low velocity case, in agreement with the experimental results. **(D)** Force versus distance profiles for different velocities conditions.

## C. Simulated results for initial conditions of 30 deg angular mismatch angle

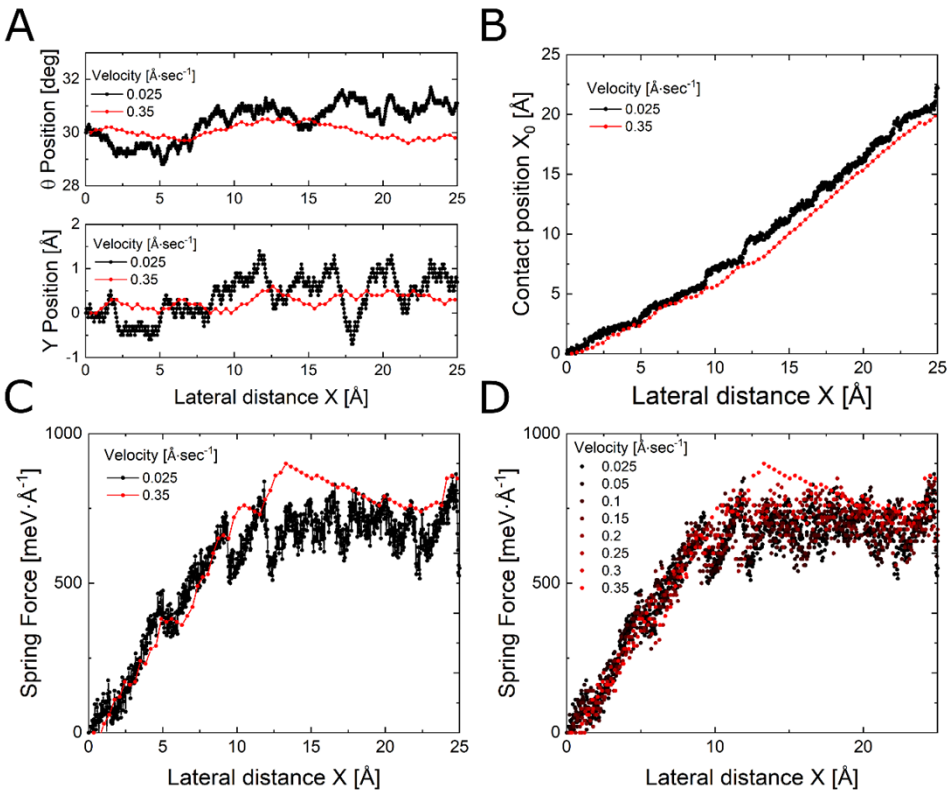


Supplementary Figure 6: Simulated results for different velocities conditions for 100 Å diameter bilayer graphene interface during shearing from the center position (full overlap). The initial misfit angle and the Y-position offset were set to 30 deg and zero, respectively. **(A)** Y-position and rotation misfit angle θ during the slide. **(B)** $x_0$-position of the top flake during the slide. At low velocity of 0.025 Å·sec$^{-1}$, the spring tends to jump forward earlier during the slide and therefore it is overall more relaxed compared to high velocity case of 0.35 Å·sec$^{-1}$. **(C)** Force versus distance profile, where the force profile of the higher velocity case follows the maximal values of the low velocity case, in agreement with the experimental results. **(D)** Force versus distance profiles for different velocities conditions.

References:


1. E. Koren, E. Lortscher, C. Rawlings, A. W. Knoll, U. Duerig, Adhesion and friction in mesoscopic graphite contacts. *Science* **348**, 679–683 (2015).

2. A. Kolmogorov, V. Crespi, Registry-dependent interlayer potential for graphitic systems. *Phys. Rev. B* **71** (2005).

3. M. Dienwiebel, G. S. Verhoeven, N. Pradeep, J. W. M. Frenken, J. A. Heimberg, H. W. Zandbergen, Superlubricity of Graphite. *Phys. Rev. Lett.* **92** (2004).

4. C. Lee, X. Wei, J. W. Kysar, J. Hone, Measurement of the Elastic Properties and Intrinsic Strength of Monolayer Graphene. *Science* **321**, 385–388 (2008).

5. D. Dutta, A. Oz, O. Hod, E. Koren, The scaling laws of edge vs. bulk interlayer conduction in mesoscale twisted graphitic interfaces. *Nat. Commun.* **11**, 4746 (2020).